

Role of the basin boundary conditions in gravity wave turbulence

L. Deike¹, B. Miquel², P. Gutiérrez³, T. Jamin¹, B. Semin²,
S. Aumaître³, M. Berhanu¹, E. Falcon^{1†}, and F. Bonnefoy⁴

¹Univ Paris Diderot, Sorbonne Paris Cité, MSC, UMR 7057 CNRS, F-75 013 Paris, France

²Ecole Normale Supérieure, LPS, UMR 8550 CNRS, F-75 205 Paris, France

³CEA-Saclay, Sphynx, DSM, URA 2464 CNRS, F-91 191 Gif-sur-Yvette, France

⁴Ecole Centrale de Nantes, LHEEA, UMR 6598 CNRS, F-44 321 Nantes, France

(Received 1 January 2019)

Gravity wave turbulence is studied experimentally in a large wave basin where irregular waves are generated unidirectionally. The role of the basin boundary conditions (absorbing or reflecting) and of the forcing properties are investigated. To that purpose, an absorbing sloping beach opposite to the wavemaker can be replaced by a reflecting vertical wall. We observe that the wave field properties depend strongly on these boundary conditions. Quasi-one dimensional field of nonlinear waves propagate before to be damped by the beach whereas a more multidirectional wave field is observed with the wall. In both cases, the wave spectrum scales as a frequency-power law with an exponent that increases continuously with the forcing amplitude up to a value close to -4 , which is the value predicted by the weak turbulence theory. The physical mechanisms involved are probably different according to the boundary condition used, but cannot be easily discriminated with only temporal measurements. We have also studied freely decaying gravity wave turbulence in the closed basin. No self-similar decay of the spectrum is observed, whereas its Fourier modes decay first as a time power law due to nonlinear mechanisms, and then exponentially due to linear viscous damping. We estimate the linear, nonlinear and dissipative time scales to test the time scale separation that highlights the important role of a large scale Fourier mode. By estimation of the mean energy flux from the initial decay of wave energy, the Kolmogorov-Zakharov constant is evaluated and found to be compatible with a recent theoretical value.

1. Introduction

Oceanic surface is characterized by the propagation of gravity waves generated by the interaction between the wind and a liquid surface (Janssen 2004). As the wind distribution over the ocean is inhomogeneous and erratic, forecasting of a sea state remains a complex problem. Once generated, the wave field evolves itself due to interactions between nonlinear waves, wave dispersion and dissipation. In particular, when wave amplitudes are high enough, a regime of wave turbulence can be observed, where wave field displays a continuous wave spectrum from large to small scales, typically from 100 m to 10 m (Hwang *et al.* 2000). Wave turbulence theory in its weakly nonlinear limit, also called weak turbulence, yields a theoretical framework to study wave turbulence regimes. This theory provides, for idealistic conditions, an analytical derivation of the spectrum of waves in a turbulent regime in almost all fields of physics involving waves (Zakharov *et al.* 1992; Newell & Rumpf 2011; Nazarenko 2011). This theory consists of

† Email address for correspondence: eric.falcon@univ-paris-diderot.fr

a weakly nonlinear development of a random field of waves propagating without dissipation in an infinite system. For gravity waves, the spectrum of wave amplitude $S_\eta(f)$ is predicted to scale as a frequency-power law in f^{-4} , and reads (Zakharov & Filonenko 1967a; Zakharov & Zaslavsky 1982)

$$S_\eta(\omega) = C\epsilon^{1/3}g\omega^{-4}, \quad (1.1)$$

with ϵ the mean energy flux, g the acceleration of gravity, $\omega = 2\pi f$, and C the non dimensional Kolmogorov-Zakharov constant. As the hypotheses used are too restrictive to be all verified experimentally, it seems unlikely that wave turbulence theory can alone explain dynamics of ocean surface. Nevertheless, this theory can give insights on the mechanisms at play. *In situ* observations provide ocean surface measurements for different wind forcing conditions. It led to several phenomenological descriptions of the wave spectrum that depend on numerous parameters such as duration of wind blowing, wind directionality, fetch length, stage of storm growth and decay, existence of a swell, *etc.* (Ochi 1998). As a consequence, *in situ* measurements of the wave spectrum varies considerably according to the conditions and locations of observations (Liu 1989; Banner 1990). However, certain measurements of the spectrum are compatible with a f^{-4} scaling (Donelan *et al.* 1985; Forristall 1981; Kahma 1981; Toba 1973; Hwang *et al.* 2000) thus suggesting a possible agreement with weak turbulence theory at large scale (wavelengths $10 \lesssim \lambda \lesssim 100$ m). At smaller scales ($\lambda < 10$ m), a transition to a steeper spectrum in f^{-5} is reported (Long & Resio 2007; Forristall 1981; Romero & Melville 2010), known as a “saturation range spectrum” or the Phillips’ spectrum (Phillips 1958; Kitaigorodskii 1983). Occurrence of this steeper spectrum may be caused by wave breakings dissipating all the injected power and by gravity-capillary wave conversion whereas the location of transition scale depends on the wind intensity. But as meteorological conditions are by nature variable and precise measurements on ocean surface are difficult, description of this transition between these two kinds of spectra remains an open question. Moreover, the frequency power-law exponent of the spectrum has also been found to depend continuously on the wave steepness (Huang *et al.* 1981). Laboratory experiments in large wave basins could be therefore useful to better understand out-of-equilibrium spectra of wave elevation in absence of wind forcing, by studying dynamics of gravity waves produced by wavemakers in well-controlled conditions.

2. State of the art about gravity wave turbulence in laboratory

We limit ourself here to laboratory experiments on gravity wave turbulence forced by vibrating blades with no wind generation. Recently, several well-controlled experiments have been carried out to test specifically wave turbulence theory for gravity waves on the surface of water (Falcon *et al.* 2007b; Denissenko *et al.* 2007; Herbert *et al.* 2010; Nazarenko *et al.* 2010; Cobelli *et al.* 2011; Issenmann & Falcon 2013). Main parameters of these experiments are sum up in table 1 for comparison. The wave spectrum is usually inferred from a capacitive or resistive gauge measuring the temporal wave elevation $\eta(t)$ at a certain location. It is defined as the square modulus of the Fourier transform of $\eta(t)$ over a duration T ,

$$S_\eta(f) \equiv \frac{1}{2\pi T} \left| \int_0^T \eta(t) e^{i\omega t} dt \right|^2, \quad (2.1)$$

with $\omega = 2\pi f$. At high enough forcing, the spectrum is found to scale as f^α within an inertial range corresponding to gravity wave scales (typically from the forcing scales to centimeter). In most of these experiments in table 1, α is found to increase with forcing

	Paris1	Paris2	Paris3	ParisA	Hull	Nantes
Basin size L or $L \times l$ (m) Geometry	0.2 circular	0.2 circular	0.5×0.4 rect.	1.8×0.6 rect.	12×6 rect.	15×10 rect.
Forcing mechanism	pistons	horizontal	pistons	pistons	pistons	pistons
Forcing freq. bandwidth (Hz)	2 - 6	1 - 7	1 - 4	0-1.5/0-4	1 - 1.15	1 -1.15
Max. spectrum freq. f_m (Hz)	4	4	3	3	1.1	1.1
Forcing wavelength λ_m (m)	0.1	0.1	0.2	0.2	1.4	1.4
Wave steepness $k_m \times \sigma_\eta$	-	0.01 - 0.1	-	-	0.08 - 0.25	0.05 - 0.25
L/λ_m	2	2	2	9	9	11
Piston-gauge distance	$0.7\lambda_m$	λ_m	λ_m	-	$4.3\lambda_m$	$5.3\lambda_m$
Exponent α for an increasing forcing	-7 to -4	-4.5 ± 0.2	-7 to -4	-6 to -5 -4 ± 1	-6.2 to -4	-8 to -3.5

Table 1: Previous laboratory experiments on stationary gravity wave turbulence. Wave spectrum $S_\eta(f)$ scales as f^α with α depending on the forcing amplitude for several experimental conditions. Paris1 (Falcon *et al.* 2007*b*), Paris2 (Issenmann & Falcon 2013), Paris3 (Herbert *et al.* 2010), ParisA (Cobelli *et al.* 2011), Hull (Denissenko *et al.* 2007; Nazarenko *et al.* 2010), and Nantes (this article). Working fluid: water except in Paris1 (water or mercury).

amplitude for all the basin sizes used (ranging from 20 cm to 15 m), and even when using a low viscosity working fluid such as mercury. When the forcing increases, α increases roughly from -7 to saturate close to -4 , the value expected theoretically by weak turbulence. However, this dependence on the forcing amplitude is in strong disagreement with theory. If instead of using a spatially localized forcing (vibrating blades), the whole container is horizontally vibrated (spatially extended forcing), α is found to be independent of the wave steepness on one decade (Issenmann & Falcon 2013). This suggests that the previous discrepancy could be related to the inhomogeneity and anisotropy of the localized forcing. However, the inertial range in the horizontally vibrated experiment remains quite small to be fully confident.

Measurements of wave elevation resolved in time and 1D space have then been performed to better resolve the wave field dynamics (Nazarenko *et al.* 2010). Both the wavenumber and frequency power law spectra are found to be dependent on the wave strength. Then, fully resolved in time and 3D space measurements have been achieved (Herbert *et al.* 2010). The spatial and temporal spectrum scalings are also found in strong disagreement with the predictions. Presence of strongly nonlinear wave propagation (such as bound waves) have been highlighted leading to a deviation from the linear dispersion relation. As a direct consequence, inferring the spatial k -spectrum from the temporal f -spectrum by using this dispersion relation yields spurious results. Finally, experiments have underlined the influence of the forcing frequency bandwidth (Cobelli *et al.* 2011). Indeed, for a narrow forcing frequency bandwidth, the dispersion relation is found to stay close to the linear one with no bound waves, and k - and f - spectra seems to be compatible with wave turbulence theory. However, the inertial range of the power-law spectrum is less than half a decade, and for a small forcing amplitude range. Note that the probability distribution of random gravity wave elevation, and the role of the forc-

ing directionality have been also studied in large wave tank but without discussing the scaling of the spectrum tail (Onorato *et al.* 2009).

Several causes have been given to explain the forcing amplitude dependent spectrum exponent. First, finite size effects could occur. Some wavelengths are quantified in finite size systems, and the resonant nonlinear wave interactions used in the theoretical derivation are replaced by quasi-resonances (Kartashova 1998; Zakharov *et al.* 2005; Lvov *et al.* 2006). Depletion of pure resonances causes the turbulent transfer through the scales to theoretically become slower and the spectrum steeper (Nazarenko 2006). However, by comparing existing experiments in table 1, we do not notice significant differences on α which can be ascribed to finite size effects for all values of basin sizes, of ratio between the typical forcing wavelength to the basin size, and of piston-gauge distance. Second, the presence of strong nonlinear waves may also explain the discrepancy with the theory. For instance, sharp crested waves, propagating breaking waves, bound waves or vertical splashes generally occur at different scales and could induce an additional dissipation acting at all scales within the inertial range. These singular coherent structures have a broad signature in Fourier spaces. Indeed, the spectrum of singularities propagating without deformation ($\omega \sim k$) scales theoretically as f^{-3-D} where $0 \leq D < 2$ is the spatial fractal dimensionality of the coherent structure (Connaughton *et al.* 2003). For instance, if sharp-crested structures occur along ridges ($D = 1$) then their spectrum scales as f^{-4} (Kuznetsov 2004). Note that this exponent is similar to the one computed by weak turbulence theory (where no crested waves are involved). In the same way, when these wave slope divergences are assumed to be isolated peaks or cusps ($D = 0$) distributed isotropically and propagating as $\omega = \sqrt{gk}$, the f^{-5} Phillips' spectrum is found again. Experimentally, it has been shown that intermittency occurs in gravity wave turbulence (Falcon *et al.* 2007a; Nazarenko *et al.* 2010), and is enhanced by coherent structures such as wave breakings (Falcon *et al.* 2010b). Third, strongly nonlinear waves involved in laboratory experiments may also lead to non-local interactions in k -space, dissipation at all scales of the cascade (energy flux not conserved), and no scale separation between linear, nonlinear and dissipating time scales unlike weak turbulence hypotheses. Finally, it has been recently reported in different experimental systems of wave turbulence that increasing dissipation leads to a spectrum that departs from weak turbulence prediction (Humbert *et al.* 2013; Miquel *et al.* 2014; Deike *et al.* 2014). Note that several numerical simulations of gravity wave turbulence validated the weak turbulence derivation (Onorato *et al.* 2002; Pushkarev *et al.* 2003; Dyachenko *et al.* 2004; Yokoyama 2004; Lvov *et al.* 2006; Korotkevitch 2008). Limited inertial range (no larger than one decade), nonlinearity truncation, and artificial numerical dissipation at large scales are the main drawbacks to go further to compare simulations and observations on gravity wave turbulence.

Previous laboratory experiments on gravity wave turbulence have been carried out in close basins whereas oceans are open systems even for the largest wavelengths. The reflecting boundary condition used in laboratory changes significantly the wave field dynamics with respect to the oceanographic situation. Indeed, wave mixing is increased and counter-propagating waves generate strong splashes in laboratory experiments.

In this article, we report an investigation of gravity wave turbulence in a large basin using accurate wave probes. We observe a power-law wave spectrum on almost two decades in frequency, one decade in the gravity range and one in the capillary range. Starting with a closed basin, we confirm previous results on gravity wave turbulence, and extend them to larger inertial range as well as various experimental parameters (see last column of table 1). Then proceeding with the same basin but with an absorbing boundary condition (beach), we observe similar frequency scalings of the wave spectrum as the

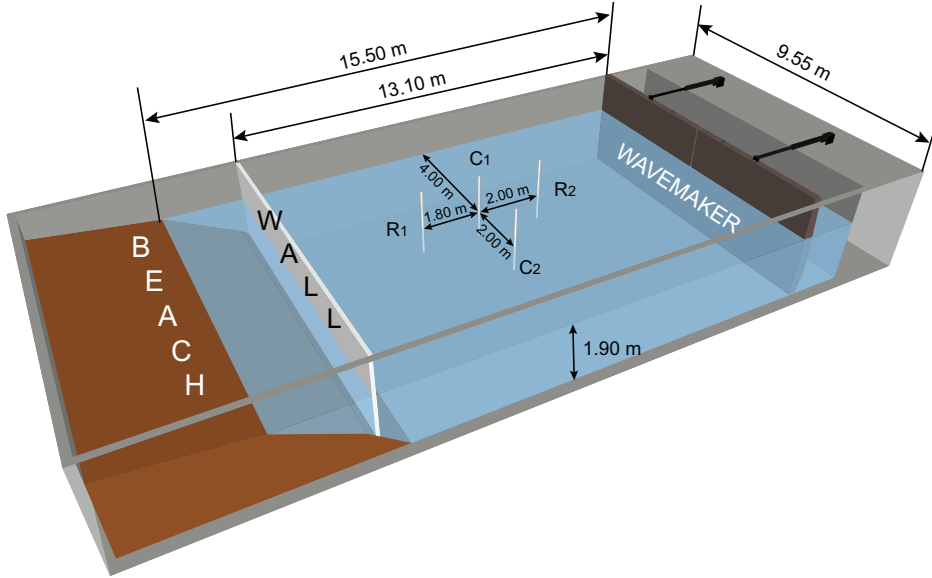


Figure 1: Sketch of the wave basin. The wavemaker is located on a side wall. The boundary opposed to the wavemaker is either a beach or a removable wall. The location of the array of probes is visible: capacitive probes C_1 and C_2 , and resistive ones R_1 and R_2 .

ones observed in the closed basin. Although direct observations of the wave field are found very different for the closed or open basin, the frequency spectra are found to depend on the forcing amplitude with the same trend in both cases. We underline that the physical mechanisms leading to these spectra are likely different, and in both cases cannot be only described by weak turbulence theory (interaction between weakly nonlinear resonant waves). In Sect. 6, intermittency properties of gravity wave turbulence are quantified. Roughly, the same value of the intermittency coefficient is found in presence of a beach or a wall, suggesting the importance of the coherent structures in both cases. Finally, in Sect. 7, we study the non-stationary regime of gravity wave turbulence during its free decay. No self-similar decay is observed in the gravity regime (the frequency power-law exponent of the instantaneous spectrum being dependent on time). We also show that the spectrum Fourier mode amplitudes first decay as a time power law in $t^{-1/2}$ (as found experimentally by Bedard *et al.* (2013b) and predicted theoretically for 4-wave interaction systems), and then decrease exponentially in time due to viscous damping. The linear, nonlinear and dissipative time scales are then inferred at all scales of the cascade. The time scale separation are then tested, and highlights the important role of a large scale Fourier mode (near the forcing scale) for gravity wave turbulence in large basins. By estimation of the mean energy flux from the initial decay of wave energy, the Kolmogorov-Zakharov constant is experimentally evaluated for the first time, and found to be compatible with a theoretical value estimated by Zakharov (2010).

3. Experimental setup

3.1. Basin and wave generation

The experiments have been performed in a large rectangular wave basin, $15\text{ m} \times 10\text{ m}$, at the Ecole Centrale de Nantes, France. The basin is filled with water with a uniform depth fixed at 1.90 m. Surface waves are generated by a rectangular flap wavemaker, 10

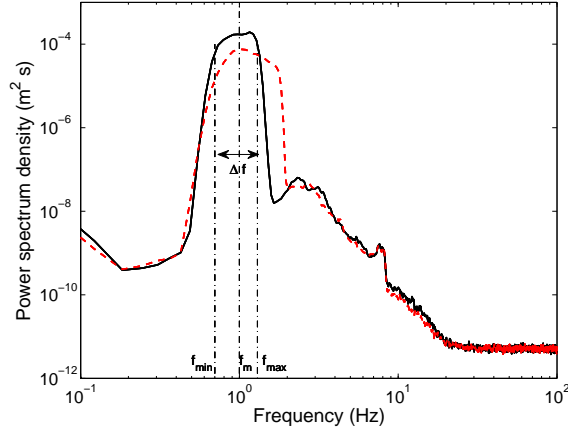


Figure 2: Power spectrum density of wavemaker displacement. Filtered random noise (—) and Jonswap (---) forcings for a broad frequency bandwidth $\Delta f = f_{max} - f_{min}$. See table 2 for corresponding forcing parameters.

m in width. It is located at one basin width as shown in figure 1. This flap is moved by hydraulic cylinders, driven in-phase and controlled by a computer. The wavemaker has a frequency cut-off at 2 Hz due to mechanical parts. A linear variable displacement transducer (LVDT) is fixed on the wavemaker top to infer its temporal displacement especially to feedback control the wavemaker position with respect to a prescribed shape spectrum.

The wavemakers generate irregular waves randomly distributed in amplitude and in frequency within a certain bandwidth. Wavemakers are driven either by a bandpass filtered random noise (FRN) within a bandwidth Δf around a frequency f_m or by a unidirectional Jonswap spectrum (JON - see figure 2). This latter has been used in oceanography to model the wave energy in the frequency domain, and based on a parametrization of the wave spectrum measurements into the North Sea (see Komen *et al.* 1994). In both cases, the forcing parameters are controlled by the frequency bandwidth Δf of the spectrum around its maximal value of frequency f_m , and by the wavemaker amplitude. Instead of the latter, we will use in the following the value of the rms wave amplitude $\sigma_\eta \equiv \sqrt{\overline{\eta^2(t)}}$ at the gauge locations (temporal average denoted by $\overline{\quad}$). Typically, one has $f_m \approx 1$ Hz (corresponding to a wavelength $\lambda_m \approx 1.5$ m), $0.3 \leq \Delta f \leq 1.3$ Hz, and $0.5 < \sigma_\eta < 7$ cm. Two typical frequency bandwidths of forcing will be considered afterwards: narrow banded for $\Delta f < 0.5$ Hz, and broad banded for $\Delta f \geq 0.5$ Hz. The forcing parameters are summarized in table 2.

The typical power spectrum density of wavemaker displacement is shown in figure 2 for a broad band forcing. It is computed from the displacement sensor fixed on the wavemaker top. No significant change is observed on the spectrum shape when changing the forcing type (JON or FRN), whereas the frequency bandwidth and the amplitude of the spectrum peak are well controlled by Δf and σ_η , respectively. Thus, the forcing type (JON or FRN) will not be distinguished in the discussion.

3.2. Boundary conditions

Two boundary conditions have been tested as sketched in figure 1. First, the wave basin is equipped with an absorbing sloping beach at one side of the basin, opposite to the

Forcing type	Parameters	Broad	Narrow
Filtered random noise (FRN)	Peak frequency f_m	1 Hz	1.15 Hz
	Bandwidth Δf	0.6 Hz	0.3 Hz
	f_{min}, f_{max}	0.7, 1.3 Hz	1, 1.3 Hz
	Wave amplitude σ_η	0.7 - 6.5 cm	0.7 - 5.0 cm
Jonswap (JON)	Peak frequency f_m	1 Hz	1.15 Hz
	Bandwidth Δf	0.6 Hz	0.4 Hz
	f_{min}, f_{max}	0.7, 1.3 Hz	0.9, 1.3 Hz
	Wave amplitude σ_η	1.3 - 3.2 cm	1.3 - 3.2 cm

Table 2: Forcing parameters to generate a prescribed spectrum of wavemaker displacement with a spectral shape (JON or FRN), a frequency bandwidth $\Delta f = f_{max} - f_{min}$, and a maximum spectrum amplitude at frequency f_m (see figure 2). The corresponding wavelengths are $\lambda_m \approx 1.5$ m (broad) and 1.2 m (narrow), respectively.

wavemakers, in order to strongly reduce wave reflections. The beach is a porous beach made of stones with a weak slope of the order of 1/3 on the firsts 3.2 meters, the lasts 3.5 meters being almost flat. This enables wave absorption by wavebreakings and porosity. Reflections amplitude are estimated to be less than 10% after 5 min of irregular waves of peak period of 1 s (Bonnetoy 2005). Thus, waves propagate up to the beach with almost no reflections going back ($< 10\%$). This boundary condition will be called afterwards *absorbing boundary condition*. The second configuration consists of a wooden wall vertically fixed in the wave basin in front of the beach (see figure 1). This case, called the *reflecting boundary condition*, corresponds to a closed basin, a situation already tested in previous laboratory experiments on gravity wave turbulence of various basin sizes (Falcon *et al.* 2007b; Herbert *et al.* 2010; Cobelli *et al.* 2011; Denissenko *et al.* 2007; Nazarenko *et al.* 2010; Bedard *et al.* 2013a,b). We will show in the following that the boundary conditions will play an important role on the dynamics of the wave field.

3.3. Wave gauges

We use an array of four wave gauges (two capacitives and two resistives) to measure the wave amplitude, $\eta(t)$, as a function of time with a sampling frequency of 500 Hz during typically $T = 10$ or 19 min. Resistive gauges are 80 cm in height. Their vertical resolution is about 0.1 mm, and their frequency resolution is close to 10 Hz (Bonnetoy 2005). The capacitive gauges are 60 cm in height and are homemade (Falcon *et al.* 2007b). Their vertical resolution is about 0.1 mm and the frequency resolution up to 200 Hz. The location of the probe array in the basin is shown in figure 1. They are located in the middle of the basin, 7.5 m from the wavemakers, corresponding to a distance of $5\lambda_m$ for the smallest value of f_m used. The measurement can be thus considered “far” from the wavemaker with respect to previous experiments in table 2 where the basin size was of the order of λ_m (Falcon *et al.* 2007b; Herbert *et al.* 2010; Cobelli *et al.* 2011). We have also verified that the wave spectrum measured in the vicinity of the wavemaker is different from the one measured in far field in the center of the basin. All results obtained here are found to be independent of the gauge type in the working range of the gauges, and of the spectral shapes prescribed to the wavemaker.

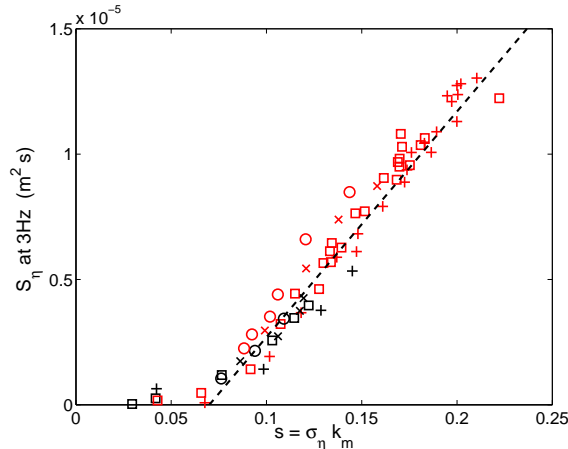


Figure 3: Amplitude of the wave spectrum amplitude $S_\eta(f)$ measured at $f = 3$ Hz as a function of mean wave steepness s . Dashed line has a slope 1. Forcing parameters: broad bandwidth ($f_m = 1$ Hz, $\Delta f = 0.6$ Hz) for FRN (\square) or JON (\circ) forcings; narrow bandwidth ($f_m = 1$ Hz, $\Delta f = 0.3$ Hz) for FRN ($+$) or JON (\times) forcings.

3.4. Wave amplitude parameter

Several parameters have been used in the literature to quantify the irregular wave amplitude. A natural choice is the rms wave amplitude, σ_η , a value directly related to the area under the wave spectrum, $S_\eta(f)$. In oceanography, the significant wave height H_s or $H_{1/3}$ was traditionally defined as the mean wave height (trough to crest) of the highest third of the waves. Nowadays, it is usually defined as $H_s = 4\sigma_\eta$, and with this choice H_s and σ_η are equivalent. The mean injected power by the wavemakers within the system has been also used previously. However, an unknown amount of energy is injected into the bulk and not into the waves (Deike *et al.* 2014). The mean wave steepness (or wave slope) s is useful to quantify the degree of nonlinearity of the wave field. It is usually defined as $s \equiv \sigma_\eta k_m$, with k_m the wavenumber corresponding to the maximum amplitude of the spectrum. In all our experiments, k_m is roughly constant, and is located in the forcing range $k_m = 2\pi/\lambda_m \approx 4.2 \text{ m}^{-1}$. The range of the nonlinearity parameter is $0.02 < s < 0.25$. The value of the spectrum amplitude at the beginning of the cascade but outside the forcing frequency range is a more relevant parameter (Nazarenko *et al.* 2010). Indeed, since the conversion between the energy given by the forcing towards the turbulent cascade is not trivial, this spectrum amplitude is a relevant parameter to quantify the amplitude of the cascade of gravity wave turbulence. For instance, for a forcing frequency bandwidth close to 1 Hz, the amplitude of the wave spectrum measured at 3 Hz corresponds roughly to the beginning of the cascade of gravity wave turbulence, and is also well separated from the first harmonic of the forcing. In the following, we will choose the spectrum amplitude at 3 Hz, $S_\eta(3\text{Hz})$, as the parameter that characterizes the forcing amplitude. As shown in Fig. 3, we found that this parameter increases monotonically with the mean wave steepness but not with a simple scaling (nonlinearly at small s , then linearly at high s). However, this relationship does not depend on the basin boundary conditions.

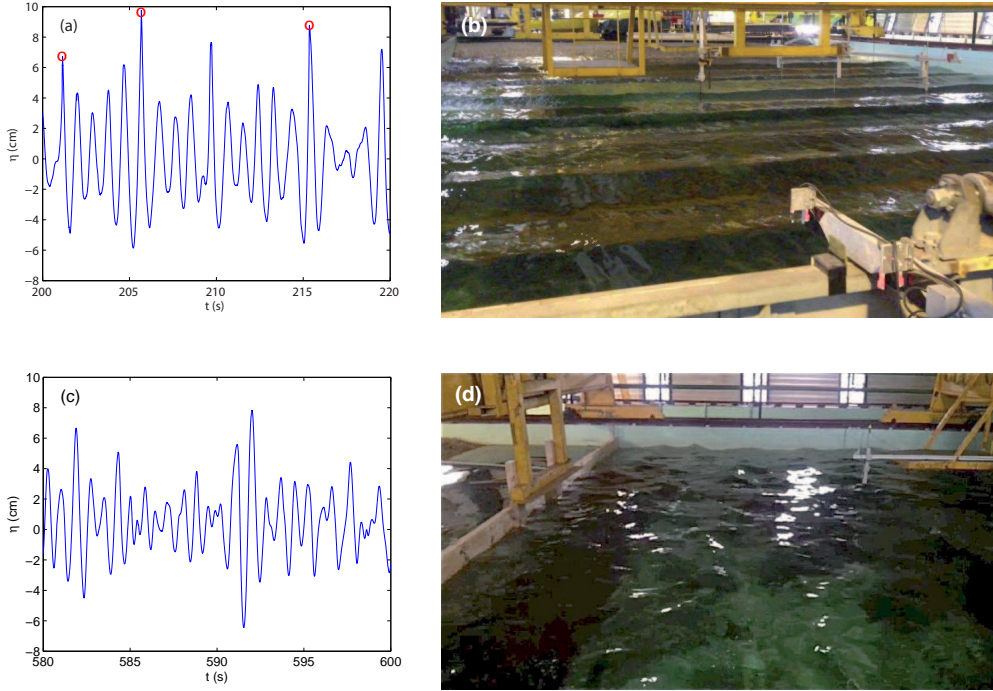


Figure 4: Typical temporal evolution of the wave amplitude $\eta(t)$ (left), and the corresponding wave field picture (right) for two different boundary conditions: beach [top - (a) and (b)] or wall [bottom - (c) and (d)]. The array of probes, the beach, and a part of the wavemaker are visible in (b). The wall is visible in (d), the shot angle being different. \circ -marks in (a) corresponds to sharp crest events. Broad bandwidth ($f_m = 1$ Hz, $\Delta f = 0.6$ Hz) for FRN forcing. $\sigma_\eta = 2$ cm (top) and 2.9 cm (bottom).

4. Role of basin boundary conditions on wave field

We focus here on the influence of the basin boundary conditions on the wave field in the real space.

4.1. Direct observation of the wave field

Irregular waves (random in frequency and amplitude) are generated by the wavemakers as explained in Sect. 3. The typical temporal evolution of wave amplitude $\eta(t)$ and the corresponding picture of the wave field in a stationary regime are shown in Fig. 4 for two different boundary conditions: beach (top) or wall (bottom). The direct observation of the wave field shows that its spatial structure depends strongly on the absorbing or reflecting boundary condition. In the absorbing case (beach), a quasi-one dimensional field of nonlinear waves propagate from the wavemakers before to be damped by the beach (see Fig. 4b). In the reflecting case (wall), such coherent structures are not visible. Instead a multidirectional wave field is observed (see Fig. 4d) due to nonlinear interactions between waves and due to multiple reflexions occurring on the basin walls. Note that the direction of forcing is one-dimensional in both cases, and the wave steepnesses are of the same order. The temporal evolution of the wave amplitude $\eta(t)$ are shown in figures 4a and 4c. Both signals are erratic showing rare large wave events, as well as higher frequency components than the forcing ones. Note that sharp crest

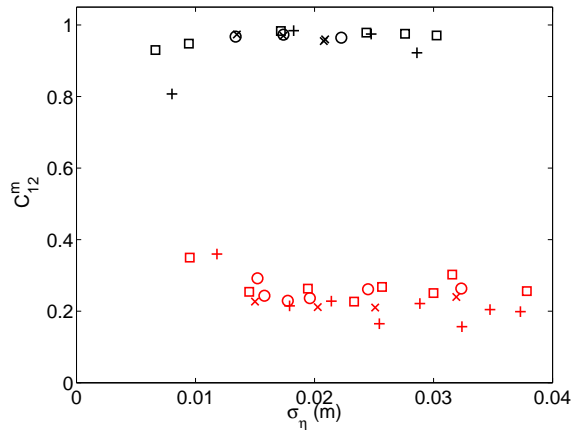


Figure 5: Maximum of correlation amplitude, $C_{1,2}^m$, between the wave gauges 1 and 2 as a function of rms wave amplitude, σ_η , for two different boundary conditions: absorbing (beach - black) and reflecting (wall - red light grey). Symbols correspond to the same forcing parameters as in figure 3.

events seems more probable in the beach case (as emphasized by circles in figure 4a) whereas such events occurs more seldom with a wall (figure 4c). Both displayed samples have been checked to be representative of the whole time series for both boundary conditions. Moreover, for highest forcing amplitudes, we notice, sometimes, the presence of breaking events during the propagation similar to those studied in laboratory flumes (Melville *et al.* 2002; Perlin *et al.* 2013). At high enough forcing amplitude and for both boundary conditions, we find that the probability distribution function of wave amplitude is well described by a Tayfun distribution (the first quadratic nonlinear correction to the Gaussian) (Tayfun 1980; Socquet-Juglard *et al.* 2005) as already found in laboratory experiments (Onorato *et al.* 2004; Falcon *et al.* 2007b; Onorato *et al.* 2009; Falcon & Laroche 2011) or in oceanography (Ochi 1998; Forristall 2000).

4.2. Spatial correlation of the wave field

We compute the spatial correlation between the wave gauges to quantify the basic spatial properties of the wave field. The correlation between the wave gauge i and j reads $C_{ij}(\tau) = \lim_{T \rightarrow \infty} \frac{1}{T} \int_{-T}^T \eta_i(t) \eta_j(t+\tau) dt / \sqrt{C_{ii} C_{jj}}$ where $C_{ii} = \lim_{T \rightarrow \infty} \frac{1}{T} \int_{-T}^T \eta_i(t) \eta_i(t+\tau) dt$ is the autocorrelation function. The correlation function is thus normalized between -1 and 1 . The maximum over the time τ of the correlation, C_{ij}^m , gives information on the wave field mixing and propagation properties between the gauges. $C_{ij}^m = 1$ occurs when signals from gauges i and j are totally correlated, while $C_{ij}^m = 0$ corresponds to two signals completely uncorrelated. Note that the correlation between two gauges depends on the linear dispersion of a wave packet, the propagation direction of the waves as well as decorrelation induced by nonlinear interactions.

Figure 5 shows the maximum of correlation amplitude, $C_{1,2}^m$, between two probes facing the wavemaker (wave gauges C1 and C2). These probes are located at the same distance of the wavemaker and are separated by 2 m (see Fig. 1). The maximum correlation is reached for $\tau \simeq 0$. We found that $C_{1,2}^m$ depends strongly on the basin boundary conditions. For an absorbing condition (beach), the wave amplitudes are highly correlated whatever the forcing ($C_{1,2}^m$ close to 1), while for reflecting boundary condition (wall), the correlation is low ($C_{1,2}^m < 0.4$). A two-point correlation close to 1 means that the same wave train is

observed at the two probes at the same time. This confirms quantitatively the fact that, with the beach, the wave field remains almost one-dimensional during the propagation. For the wall case, the correlation is much lower due to the multiple reflexions occurring on the basin walls enhancing nonlinear wave interactions. The resulting wave field is thus more complex as directly observed in Fig. 4d. The two-points correlation then confirm simple observation of the wave field pictures. Note that similar results are found for the correlation between two probes aligned with the forcing direction. These spatial properties obtained from temporal measurements (even if spatio-temporal ones should be ideally obtained) are mainly related to the forcing properties and to the boundary conditions. We have to keep in mind these simple spatial properties when we will discuss the wave spectrum in the next Sect. 5.

5. Role of basin boundary conditions on the wave spectrum

We now discuss the role of the boundary conditions on the wave field in the Fourier space.

5.1. Wave spectrum

Figures 6 shows the wave amplitude spectra, $S_\eta(f)$, for increasing forcing amplitudes for reflecting (a) or absorbing (b) boundary conditions. Surprisingly, both conditions lead to same qualitative shape of the spectra when the forcing is increased. For small forcing amplitude, peaks related to the forcing and its harmonics are visible in the low frequency part of the spectrum and no power law is observed. At high enough forcing, those peaks are smeared out and a power law, $S_\eta(f) \sim f^\alpha$, can be fitted. This corresponds to the cascade of gravity wave turbulence ranging on one decade in frequency from roughly 1.5 Hz (the higher forcing frequency) up to the gravity-capillary crossover frequency $f_{gc} \equiv \sqrt{2g/l_c}/(2\pi) \simeq 14$ Hz with $l_c \equiv \sqrt{\gamma/(\rho g)}$ the capillary length, $g = 9.81$ m/s² the acceleration of gravity, $\gamma = 70$ mN/m the surface tension, and $\rho = 1000$ kg/m³ the water density (Falcon *et al.* 2007b). When the forcing is further increased, the slope of the power law spectrum becomes less steep, corresponding to an increase of the exponent α . Finally, for the highest forcings, the slope seems to saturate to a constant value (see dashed line) although the peak amplitude of the forcing frequencies still increases. For both boundary conditions, this value is close to -4 the exponent predicted by gravity wave turbulence theory (Zakharov & Filonenko 1967a).

Let us now look at the high frequency part of the spectrum, corresponding to the capillary range, where the spectrum shape changes. At high enough forcing, a second power law is indeed observed on almost one decade in frequency ($f_{gc} < f < 100$ Hz). The slope is much less steep than the gravity one and is close to the capillary wave turbulence prediction in $f^{-17/6}$ (see dot-dashed lines) (Zakharov & Filonenko 1967b). Note that the observation of both direct cascades of gravity and capillary wave turbulence was hardly reachable in previous large basin facilities. It is possible here due to both the high sensitivity and low noise level of capacitive probes, the latter being reached for $f \gtrsim 200$ Hz. These results are found to be independent of the forcing parameters (spectral shape and frequency bandwidth).

As discussed in Sect. 4, the propagation of a quasi-one dimensional field of nonlinear waves is observed in presence of a beach, whereas numerous propagation directions are involved in presence of a wall leading to a multidirectional wave field. Although the wave field structure is very different according to the boundary conditions, it is very surprising that the corresponding wave spectra do not show a significant difference.

The frequency power law of the gravity wave spectrum, $S_\eta(f) \sim f^\alpha$, is found to depend

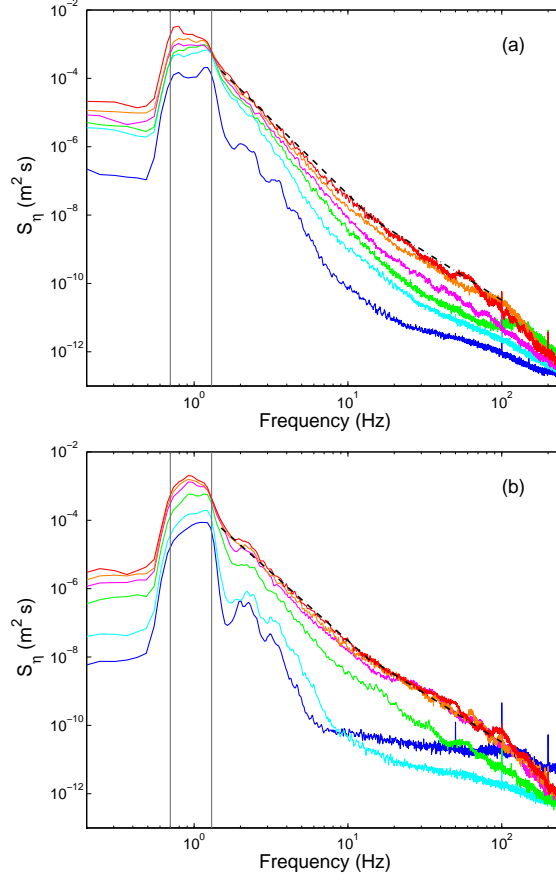


Figure 6: Power spectra of wave amplitude, $S_\eta(f)$, for reflecting (a) or absorbing (b) boundary conditions. Forcing amplitude increases from bottom to top. (a) weak turbulence predictions for gravity regime $S_\eta \sim f^{-4}$ (dashed line) and capillary regime $S_\eta \sim f^{-17/6}$ (dot-dashed line). (b): Best fit $\sim f^{-4.4}$ in the gravity regime (dashed line), and $f^{-17/6}$ in the capillary regime (dot-dashed line). Vertical grey lines show to the forcing frequency range. Same forcing parameters for (a) and (b). FRN forcing with broad bandwidth ($f_m = 1$ Hz, $\Delta f = 0.6$ Hz, and $0.6 \leq \sigma_\eta \leq 3.7$ cm).

on the forcing amplitude. Figure 7 shows α as a function of the forcing strength for both the absorbing and reflecting boundary conditions. We choose to plot it as a function of $S_\eta(3 \text{ Hz})$, the value of the spectrum amplitude at 3 Hz (a forcing strength parameter more relevant than the mean wave steepness s , or the rms wave amplitude σ_η as explained in §3.4). The exponent α is found to increase with the forcing strength for both boundary conditions. In a closed basin, α seems to saturate at high forcing near -4 within the data scattering. In presence of a beach, the highest value reached by α is also -4 but for a smaller $S_\eta(3 \text{ Hz})$. For both boundary conditions, α is thus found to be close to -4 at high enough forcing. The maximum value of $S_\eta(3 \text{ Hz})$ reached in presence of a beach is less than the one obtained with a wall for the same forcing parameters. This comes from the fact that the dissipated power is stronger in presence of a beach than within a closed basin. As said above, our results are found to be independent of the spectral shapes prescribed to the wavemaker. Finally, when comparing our results performed in

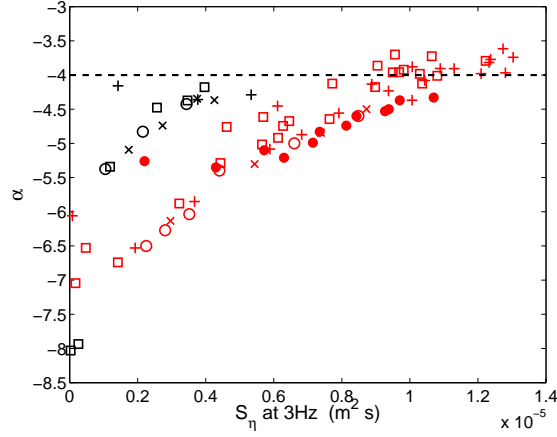


Figure 7: Frequency power-law exponent, α , of the gravity wave spectrum $S_\eta \sim f^\alpha$ as a function of the value of the spectrum amplitude at 3 Hz, $S_\eta(3 \text{ Hz})$. Boundary conditions: wall (red light grey) and beach (black). Dashed line corresponds to the prediction of weak turbulence theory $\alpha = -4$. Fit frequency range: 3 to 10 Hz. Error bar on α is ± 0.2 . Symbols correspond to the same forcing parameters as in figure 3 and $0.5 < \sigma_\eta < 5 \text{ cm}$. (●)-symbols correspond to Hull experiments of Fig. 6 (left) in Nazarenko *et al.* (2010).

the closed basin with those reported in the Hull experiments (Nazarenko *et al.* 2010) [see (●)-symbols in Fig. 7], a good overall agreement is found although a smaller value of $S_\eta(3 \text{ Hz})$ is needed in our case to reach the same value of α .

5.2. Discussion

Weak turbulence prediction for the wave spectrum in the gravity regime reads $S_\eta(f) \sim f^{-4}$ (Zakharov & Filonenko 1967a), and is shown in dashed line in Fig. 7. It seems to roughly describe the data at high enough $S_\eta(3 \text{ Hz})$ for both boundary conditions. However, one would have expected a better agreement with the data at low $S_\eta(3 \text{ Hz})$, i.e. at low wave steepness, since this theory is weakly nonlinear. Moreover, a lower $S_\eta(3 \text{ Hz})$ is needed to reach this -4 value in presence of a beach than of a wall. This could be also paradoxical since the spatial structure of the wave field in presence of a beach involves mainly unidirectional coherent structures (see Fig. 4b) whereas a multidirectional wave field is observed with a wall (see Fig. 4d), this latter situation being much closer to the isotropic assumption of weak turbulence. However, some very small correction to the -4 exponent is predicted due to anisotropy (Pushkarev *et al.* 2003), and generally swell and blowing wind are barely isotropic in oceans.

A possible explanation of the f^{-4} spectrum scaling at high enough forcing is given by the spectrum of one-dimensional spatial singularities (Kuznetsov 2004; Nazarenko *et al.* 2010). If the wave field dynamics is dominated by 1D sharp crested waves propagating with a preserved shape, as observed in the beach case, the Fourier transform of the amplitude of these singularities is $\hat{\eta}(k) \sim k^{-2}$. Its power spectrum is $S_\eta(k) \sim |\hat{\eta}(k)|^2 \sim k^{-4}$ in wavenumber, and $S_\eta(\omega) = S_\eta(k) \frac{dk}{d\omega} \sim \omega^{-4}$ in frequency, assuming a constant group velocity (i.e. $\omega \sim k$). However, our temporal measurements of the wave amplitude with a probe at a single location cannot discriminate which mechanism is involved at high forcing, either the singular coherent structures or the resonant wave interactions of weak turbulence theory. For this, full space and time resolved measurements of wave elevations are needed since coherent structures do not belong to the linear dispersion relation curve

and thus should be easily detectable. A spatio-temporal measurement of wave height working in the gravity range could be tested as the ones used for gravity-capillary wave turbulence (Herbert *et al.* 2010) or capillary wave turbulence (Berhanu & Falcon 2013; Wright *et al.* 1996). Other methods measuring surface gradient of the wave field both in space and time (see Moisy *et al.* 2009, and references therein) are intrinsically limited to weak wave steepness and will be hardly useful for such a discrimination.

One way to interpret our results at high forcing would be to ascribe the observed spectra to the propagation of coherent structures in the presence of a beach and to a weak turbulence mechanism in the presence of a wall. However, this does not explain the spectrum exponent depends on the forcing in both cases (see Fig. 7). It has been shown previously that when removing such coherent structures from the wave amplitude signal leads to a gravity spectrum exponent that still depends on the forcing but with a lesser variation of the order of 25% (Falcon *et al.* 2010*b*). Using a similar criterion to define the occurrence of wavebreaking events (time intervals where the wave acceleration is greater than 6 times its standard deviation), ones computes here the spectrum of the wave signal not including wavebreakings. We find that the spectrum exponent is only decreased by roughly 10% but still depends on the forcing, and no clear difference is observed between the wall and beach cases within our data scattering.

The relative importance of dissipation (e.g. by wavebreakings) with respect to nonlinear interactions may also explain the steepening of the gravity spectrum at low nonlinearity. In capillary wave turbulence, a similar phenomenon of steepening of the spectrum at low nonlinearity has been reported experimentally when working with high enough viscosity fluids (Deike *et al.* 2014) and numerically when reducing the nonlinear interactions (Pan & Yue 2014). The next section dealing with intermittency in wave turbulence can give insights on the mechanisms at play.

6. Role of basin boundary conditions on intermittency

The phenomenon of intermittency has been observed experimentally in gravity wave turbulence (Falcon *et al.* 2007*a*, 2010*b*; Nazarenko *et al.* 2010). Here, we wonder what is the role of the boundary conditions on the intermittency properties in gravity wave turbulence.

The intermittence of a stochastic stationary signal, $\eta(t)$, are generally tested by computing the structure functions using the first-order differences of the signal, $\eta(t+\tau) - \eta(t)$. A signal with a steep power spectrum, $S_\eta(f) \sim f^\alpha$, is locally multi-derivable, and a high-order difference statistics is then required to test intermittency (Falcon *et al.* 2010*a,b*). For instance, with $|\alpha| \geq 5$, the third-order difference statistics is at least required. Here, we found that statistical convergence of the structure functions is reached when using the fourth-order (or higher) difference statistics. The fourth-order differences of the signal $\Delta\eta_t(\tau) \equiv \eta(t+2\tau) - 4\eta(t+\tau) + 6\eta(t) - 4\eta(t-\tau) + \eta(t-2\tau)$, are thus computed in the following. $\eta(t)$ is recorded with a 500 Hz sampling rate during 19 min leading to 6×10^5 points.

The probability density functions (PDFs) of $\Delta\eta_t(\tau)$ normalized to their rms values $\sigma_{\Delta\eta}$ are displayed in figure 8a for different time lags τ and for two configurations (wall and beach). We choose the range $50 \leq \tau \leq 170$ ms corresponding to a frequency range $[2.9 \leq 1/(2\tau) \leq 10$ Hz] within the gravity regime where the wave spectrum is found to scale as a frequency power law, $S_\eta(f) \sim f^\alpha$, with $\alpha = -5$ and -4.2 for the wall and the beach, respectively. In both cases, we observe that the PDF shape changes continuously when τ is decreased (see arrows). The PDF is found to be more flattened when looking on shorter scales τ . More intense and rare events thus occur in the signal meaning that the

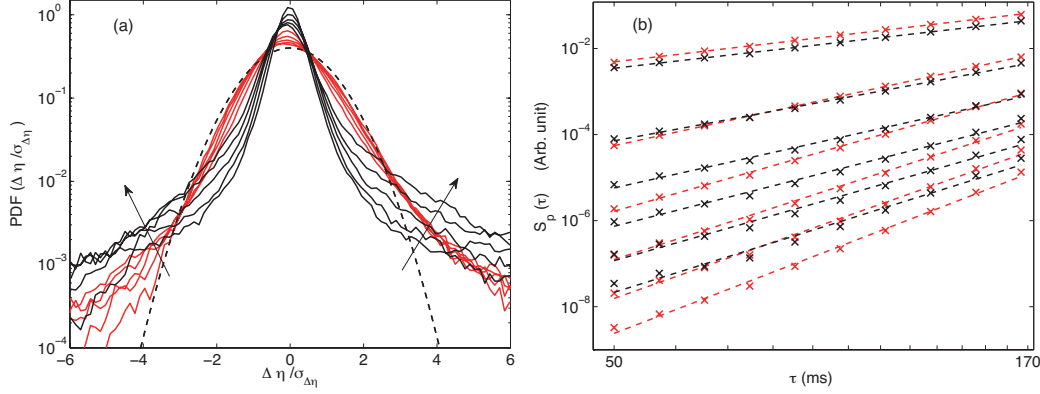


Figure 8: (a) Probability density functions of normalized increments $\Delta\eta_t(\tau)/\sigma_{\Delta\eta_t(\tau)}$ for different time lags $\tau = 50, 65, 85, 111,$ and 146 ms (see arrows) and two configurations: wall (red light grey) and beach (black). Dashed line: Gaussian with zero mean and unit standard deviation. (b) Structure functions of the fourth-order differences of the wave amplitude, $\mathcal{S}_p \sim \tau^{\zeta_p}$, as functions of the time lag τ , for $1 \leq p \leq 6$ (from top to bottom). Wall (red light grey) and beach (black). Dashed lines are corresponding power law fits which their slopes ζ_p depends on the order p (see figure 9). Same forcing parameters as in figure 4 and 6 with $\sigma_\eta = 3$ cm [$S_\eta(3 \text{ Hz}) = 10^{-5} \text{ m}^2\text{s}$ (wall) and $0.4 \cdot 10^{-5} \text{ m}^2\text{s}$ (beach)].

PDFs are more intermittent. Two other observations can be done. First, in both cases, the PDFs are not Gaussian at large τ meaning that intermittency already takes place at the forcing scales. Second, in both cases, the PDFs are asymmetric with more positive events than negative ones. This could be ascribed to the wave asymmetry (forward front are different than rear one) due to nonlinear effects. Finally, one observes that the tails of PDFs are more populated in presence of a beach than with a wall, for the same rms wave amplitude, whereas its center is much more peaked.

To quantify the intermittency, the structure functions of order p , $\mathcal{S}_p(\tau) \equiv \overline{|\Delta\eta_t(\tau)|^p}$, are computed from the fourth-order differences of the signal. $\mathcal{S}_p(\tau)$ are shown in figure 8b for both the wall and beach cases, and for comparable $S_\eta(3 \text{ Hz})$. All the structure functions of order p (from 1 to 6) are well fitted by power laws of τ , $\mathcal{S}_p(\tau) \sim \tau^{\zeta_p}$, where ζ_p is found to increase with the order p in both cases. The exponents ζ_p of the structure functions are then plotted in the main figure 9 as a function of p . ζ_p is fitted by a quadratic function of p such that $\zeta_p = c_1 p - \frac{c_2}{2} p^2$ where the values of c_1 and c_2 are found to both depend on the forcing (see top and bottom insets of figure 9). The c_1 coefficient is found to decrease from 3 to 1.7 for increasing $S_\eta(3 \text{ Hz})$, and to depend on the boundary conditions (see top inset of figure 9). This decrease of c_1 is due to the decrease of the wave spectrum exponent $|\alpha|$ with $S_\eta(3 \text{ Hz})$ (see figure 7), since both values are related by $|\alpha| = \zeta_2 + 1 = 2(c_1 - c_2) + 1$. This argument also explains the deviation between the evolutions of c_1 in the case of a wall or a beach (top inset of figure 9). The nonlinearity of ζ_p ($c_2 \neq 0$) is a signature of intermittency (Pope 2006). The so-called intermittency coefficient c_2 is found to increase from 0 up to roughly 0.4 when the forcing is increased. However, no significant difference is observed, within our data scattering, in presence of a wall or a beach. Similar results have been found when the forcing is increased.

Nazarenko *et al.* (2010) suggested that instead of fitting ζ_p by a quadratic function, ζ_p can be adjusted, for high value of p , with a linear fit to measure the fractal dimension of possible singularities involved in the wave field. For the data in the main figure 9, a

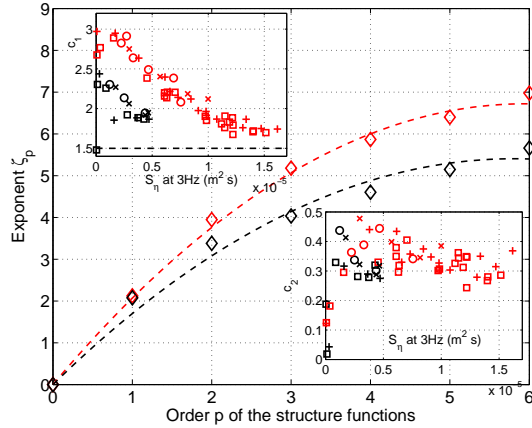


Figure 9: Exponents ζ_p of the structure functions as a function of p for wall (red light grey) and beach (black) configurations. Dashed lines are best fits $\zeta_p = c_1 p - \frac{c_2}{2} p^2$. ζ_p are inferred from the slopes of the power-law fits in figure 8b. Top and bottom insets show the evolution of c_1 and c_2 with the forcing. Symbols in the insets corresponds to same forcing parameters as in figure 3 and $0.5 < \sigma_\eta < 5$ cm [$S_\eta(3 \text{ Hz}) < 1.6 \cdot 10^{-5} m^2 s$].

linear fit of ζ_p for $p > 2$ leads to a slope of 0.55, and an intersect with the y -axis less than 2 in both cases (wall and beach). The fractal dimension inferred from these values and using Eq. (2.28) of Nazarenko *et al.* (2010) is negative, and thus raises doubts about the validity of this approach.

To conclude, we have found that the intermittency coefficient has roughly the same value in presence of a beach or a wall, but is found to strongly depend on the forcing as previously reported (Falcon *et al.* 2010b). Since it has been shown that intermittency is enhanced by coherent structures (Falcon *et al.* 2010b), our observations thus suggest that the importance of coherent structures increases with the forcing both for the beach and the wall with the same trend. The main difference concerns the PDF of increments that displays more rare and intense events in presence of a beach, and a much more peaked distribution in its center than with a wall. This probably suggests that the mixing of waves is less efficient, and intense coherent structures are more probable in presence of a beach than with a wall.

7. Decaying gravity wave turbulence in the closed basin

We present here an investigation of freely decaying gravity wave turbulence in the closed basin. Previous experimental studies of such non-stationary regimes have shown that the wave spectrum decays first rapidly as a time-power law in rough agreement with weak turbulence theory, and then exponentially for a longer time interval due to linear viscous dissipation (Bedard *et al.* 2013a,b). Direct numerical simulations of the Euler equations have been also performed in the freely decaying case of a swell wave field to show the validity of weak turbulence derivation (Onorato *et al.* 2002).

7.1. Experimental protocol

We use the same protocol as in previous studies on freely decaying wave turbulence on thin elastic plates (Miquel & Mordant 2011; Deike *et al.* 2013) or on the surface of a fluid (Deike *et al.* 2012; Bedard *et al.* 2013b,a). A typical experiment is as follows. First,

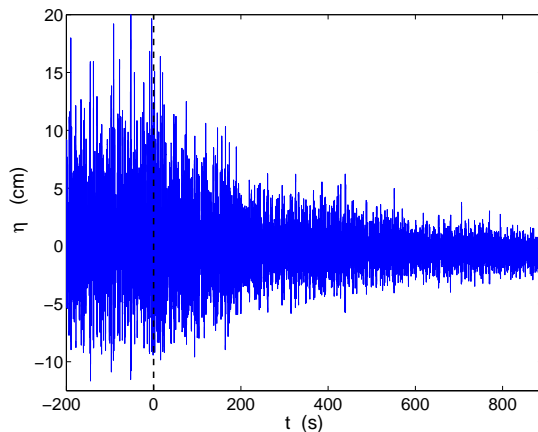


Figure 10: Decay of wave amplitude $\eta(t)$ as a function of time for reflecting boundary condition. Forcing is working for $t < 0$ and is stopped at $t = 0$. Initial forcing conditions: FRN forcing with a narrow bandwidth ($f_m = 1.15$ Hz, $\Delta f = 0.3$ Hz, $\sigma_\eta = 4.6$ cm).

surface waves are generated during 7 min, a long-enough time to reach a stationary wave turbulence state. The forcing is then stopped at $t = 0$, and the temporal decay of the wave amplitude $\eta(t)$ is recorded with a 500 Hz sampling frequency by means of two capacitive probe (C1 and C2) during 15 min, a long-enough time to observe the wave damping up to a still state. The experiment is then iterated 20 times to improve statistics, and results are averaged. Accuracy on the wavemaker stopping time is smaller than 2 s. The results are found to be independent of the locations of the probes on the 4 m probe rack. The results reported in this Section does not depend qualitatively on the initial forcing conditions used in table 2.

7.2. Temporal decay of the wave amplitude

The temporal decay of the wave amplitude $\eta(t)$ is shown in Fig. 10 for a reflecting boundary condition. $t = 0$ corresponds to the stop of the wavemakers. The decay lasts roughly 900 s including the very slow relaxation of the transverse modes of the tank. Wave energy is dissipated by viscous mechanisms (in bulk, on the free interface, and on the tank sides), and transferred to other scales by nonlinear interactions. For the absorbing boundary condition and for the same initial forcing conditions, the decay is much faster (~ 50 s roughly corresponding to the propagation time of the last generated wave train) since the beach absorbs most of the wave energy. Thus, we will only report below results on the decay within the closed basin.

7.3. Temporal decay of the spectrum

To analyze the different steps of the decay of $\eta(t)$, the time-frequency wave amplitude spectrum $S_\eta(f, t)$ is computed by means of a spectrogram analysis (MATLAB function), for each experiment on short temporal windows $[t, t + \delta t]$ with $\delta t = 8$ s, and $0 \leq t \leq 800$ s. $S_\eta(f, t)$ is then averaged first on the two probe signals, and then over 20 different realizations leading to averaged spectrum $\langle S_\eta(f, t) \rangle$, $\langle \cdot \rangle$ denoting ensemble average. Figure 11 shows $\langle S_\eta(f, t^*) \rangle$ as a function of the frequency at different decay times t^* . At the beginning of the decay (top curve), the spectrum displays a frequency-power law $\sim f^\alpha$ in the gravity frequency range ($1 \leq f \leq 10$ Hz) with an exponent α close to its value in the stationary regime. When t^* increases, the power-law spectrum is steeper and steeper, with α decreasing with time as shown in the inset of figure 11. No self-similar decay is

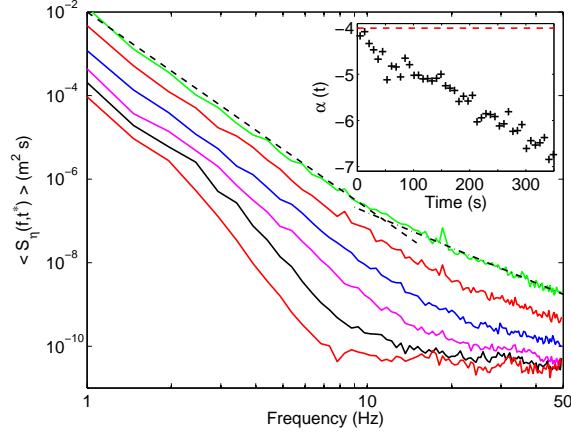


Figure 11: Wave spectrum $\langle S_\eta(f, t^*) \rangle$ at different times t^* of the decay. From top to bottom: $t^* = 25, 81, 161, 241, 401, \text{ and } 641$ s. Dashed line is a power law fit $\sim f^\alpha$ with $\alpha = -4.7$ in gravity frequency range ($1 \leq f \leq 10$ Hz). Dot-dashed line corresponds to the stationary capillary wave turbulence prediction in $f^{-17/6}$. Third top curves have been shifted vertically for clarity by a factor 10, 5, and 2, respectively. Inset: Gravity exponent α as function of time. Closed basin. Same initial forcing conditions as in Fig. 10.

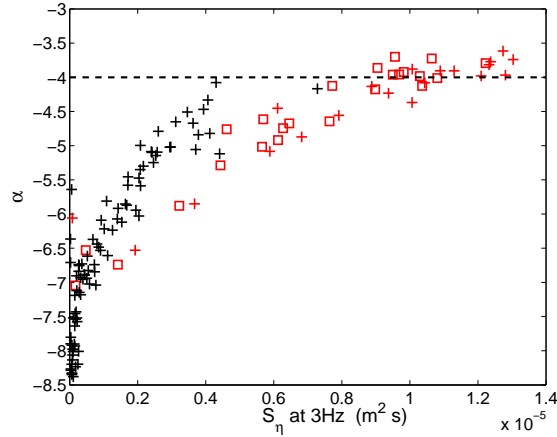


Figure 12: Frequency-power law exponent, α , of the gravity wave spectrum $S_\eta \sim f^\alpha$ as a function of the value of the spectrum amplitude at 3 Hz, $S_\eta(3 \text{ Hz})$. Decaying regime (black) or stationary regime [red (light grey)], same data as in Fig. 7]. Reflecting boundary condition. Dashed line corresponds to the prediction of weak turbulence theory $\alpha = -4$. FRN forcing with a broad (\square) or narrow (+) bandwidth.

thus observed in the gravity regime. On the contrary, in the capillary frequency range, we observe when measurements are not too noisy, that the shape of the power law spectrum does not depend significantly on the decay time. This last result is compatible with the self-similar decay of capillary wave turbulence observed previously in small container (Deike *et al.* 2012).

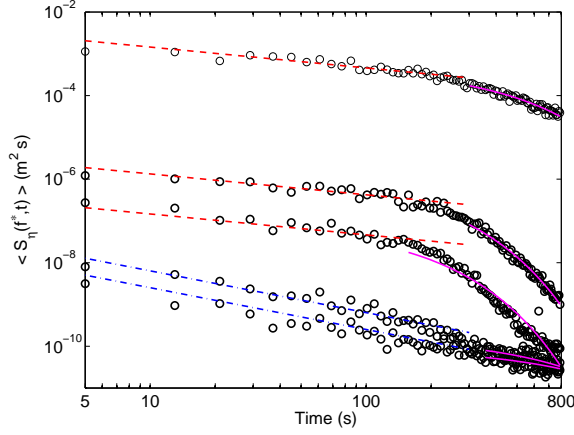


Figure 13: Temporal evolution of the wave spectrum $\langle S_\eta(f^*, t) \rangle$ for Fourier components $f^* = 1.2, 4.4, 8.3, 18.1,$ and 28.8 Hz (from top to bottom). Red dashed lines: $t^{-1/2}$ law predicted for 4-wave interactions (gravity). Blue dot-dashed lines: t^{-1} law predicted for 3-wave interactions (capillary). Solid lines: exponential decay $e^{-t/\tau_d(f^*)}$ as expected for a viscous damping, with $\tau_d(f^*)$ the damping time. Closed basin.

7.4. Frequency-power law exponent of the gravity spectrum during the decay

The frequency-power law exponent α of the spectrum is estimated within the gravity frequency range, at each instant of the decay (see inset of figure 11) and is displayed in Fig. 12 (black symbols) as a function of $S_\eta(3 \text{ Hz})$, the value of the spectrum amplitude at 3 Hz. Just after the forcing is stopped [corresponding to the highest value of $S_\eta(3 \text{ Hz})$], the exponent of the power spectrum is similar to the one observed in the stationary regime, close to -4 . During the decay, the spectrum decreases in amplitude [smaller values of $S_\eta(3 \text{ Hz})$] and is steeper (see Fig. 11). This leads to an exponent α strongly depending on $S_\eta(3 \text{ Hz})$ as shown in Fig. 12. The values of α in the decaying regime is then compared in Fig. 12 with the ones obtained in the stationary regime (red light grey symbols) of Sect. 5, both being performed in the closed basin. We observe that α increases with the spectrum amplitude both in the stationary and decaying regimes with the same trend. As a first approximation, this means that decaying wave turbulence can be seen, at each time of the decay, as a wave turbulence in a stationary regime but with the corresponding decreasing wave energy. This feature was also observed for capillary wave turbulence decay (Deike *et al.* 2012; Kolmakov *et al.* 2004). Note that the data for the decaying regime in Fig. 12 are more scattered than in the stationary regime, as the nonstationary spectra involve less statistics and thus smaller signal to noise ratio.

7.5. Temporal decay of the spectrum and energy Fourier modes

Figure 13 shows the temporal evolution of $\langle S_\eta(f^*, t) \rangle$ for different Fourier components f^* . In the first stage of the decay ($t < 200$ s), the Fourier modes in the gravity frequency range are observed to decrease in time as $t^{-1/2}$ (see dashed lines) as predicted for a nonlinear wave decay involving 4-wave interactions (Bedard *et al.* 2013a). This confirms with more accuracy the experimental $t^{-1/2}$ scaling found by Bedard *et al.* (2013b). In the capillary frequency range, the decay of the Fourier modes decrease in time as t^{-1} as expected for 3-wave interactions (Falkovich *et al.* 1995) (see dot-dashed lines). This first stage of the decay is thus related to nonlinear mechanisms. For longer decaying times ($t > 200$ s), the Fourier modes roughly decay exponentially with time as $e^{-t/\tau_d(f^*)}$, as

expected for a linear viscous dissipation. Viscous dissipation could arise from surface boundary layers on the bottom and side walls as well as on the free surface due mostly to surface contamination (Lamb 1932; van Dorn 1966; Miles 1967). The viscous damping time $\tau_d(f^*)$ is fitted empirically and is found to decrease with the Fourier mode frequency from 300 to 100 s typically. This second stage of the decay is thus driven by viscous decay of the waves.

Now, assume $E_f(t)$ the wave energy of the Fourier mode at frequency f at time t . At $t = 0$, the forcing is stopped and the decaying wave energy can be modeled by

$$\frac{dE_f(t)}{dt} = -a_1 E_f(t) - a_2 E_f^2(t) - a_3 E_f^3(t) , \quad (7.1)$$

with a_1 , a_2 and a_3 taking positive values depending on the frequency f . The first term of right-hand side corresponds to a usual viscous linear dissipation, the second and third term modeling nonlinear dissipation from 3-wave and 4-wave nonlinear interactions, respectively. These nonlinear dissipations result from the difference at a fixed frequency between the in-flux from low frequencies and the out-flux towards high frequencies. We solve this equation by considering only one non-zero dissipation coefficient a_1 , a_2 or a_3 in order to compare with a unique fit parameter the analytical solutions and the experiment results. The linear case leads to $dE_f(t)/dt = -a_1 E_f(t)$, and thus the wave energy of the Fourier mode decays exponentially in time as

$$E_f(t) = E_f(0) \exp[-t/\tau_d] , \quad (7.2)$$

with $1/\tau_d = a_1$ the linear dissipative time scale, and $E_f(0)$ the energy when the forcing is stopped. For a quadratic nonlinearity (3-wave interaction such for capillary waves), one has $dE_f(t)/dt = -a_2 E_f(t)^2$, and thus

$$E_f(t) = E_f(0) [1 + t/\tau_{nl}^c]^{-1} , \quad (7.3)$$

with $1/\tau_{nl}^c = a_2 E_f(0)$ the nonlinear decay time of capillary waves. For $t \gg \tau_{nl}^c$, one has $E_f(t) \sim t^{-1}$. Finally, for a cubic nonlinearity (4-wave interaction such for gravity waves), one obtains

$$E_f(t) = E_f(0) [1 + 2t/\tau_{nl}^g]^{-1/2} , \quad (7.4)$$

with $1/\tau_{nl}^g = a_3 E_f(0)^2$ the nonlinear decay time of gravity waves. For $t \gg \tau_{nl}^g$, one has $E_f(t) \sim t^{-1/2}$. Note that τ_d , τ_{nl}^c , and τ_{nl}^g depend on the scale f .

The temporal decay of the wave energy $E_{f^*}(t)$ at frequency f^* is related to the power spectrum of wave height at the same component, $S_\eta(f^*, t)$, by

$$E_{f^*}(t) = g S_\eta(f^*, t) + \frac{\gamma}{\rho} k^2(f^*) S_\eta(f^*, t) , \quad (7.5)$$

with $k(f)$ given by the dispersion relation of gravity-capillary linear waves.

The temporal decay of the wave energy $E_{f^*}(t)$ at each frequency f^* is thus inferred experimentally from the one of the wave spectrum, $S_\eta(f^*, t)$ – see figure 13, by using Eq. (7.5). For a fixed f^* in the gravity range ($0.5 \leq f^* \leq 10$ Hz), $E_{f^*}(t)$ is found to be well fitted at short times ($0 \leq t \leq 100$ s) by Eq. (7.4) leading thus to a experimental estimate of $\tau_{nl}^g(f^*)$, $E_f(0)$ being given by the value of σ_η in the stationary regime ($t \leq 0$). Similarly, for a fixed f^* in the capillary regime ($10 < f^* \leq 50$ Hz), $E_{f^*}(t)$ is well fitted at short times by Eq. (7.3), leading to an estimate of $\tau_{nl}^c(f^*)$. For long times ($t > 200$ s), $E_{f^*}(t)$ is found to decay exponentially as in Eqs. (7.2) in both regimes, leading thus to estimate $\tau_d(f^*)$. Finally, reiterating these fits for various f^* gives the frequency dependence of time scales τ_{nl}^g , τ_{nl}^c , and τ_d .

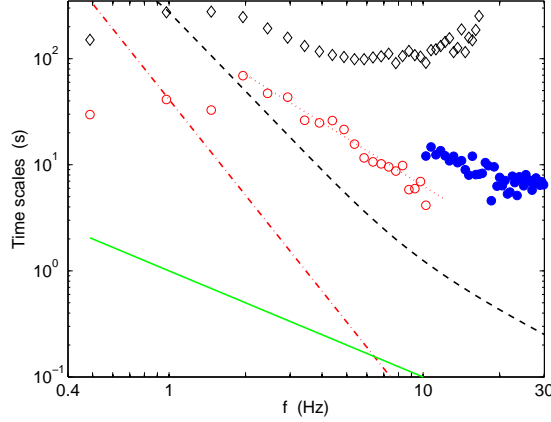


Figure 14: Typical time scales as a function of the frequency, f . Dissipative linear time scale τ_d (\diamond). Nonlinear decay times of gravity τ_{nl}^g (\circ), and capillary τ_{nl}^c (\bullet) regimes. τ_d , τ_{nl}^g , and τ_{nl}^c are inferred from fits of $E(f, t)$ [data of figure 13 using Eq. (7.5)] using Eqs. (7.2), (7.4) and (7.3), respectively. Solid line: Linear time scale $\tau_l = f^{-1}$. Red dot-dashed line: Theoretical nonlinear interaction time scale of gravity $\tau_{4w}^g \equiv c\epsilon^{-2/3}g^2f^{-3}$ (see text). Red dotted line: best fit $\sim f^{-3/2}$. Black dashed line: theoretical dissipation time scale τ_d^{theo} from Eq. (7.6) with $\nu = 10^{-6}$ m²/s. Same initial forcing conditions as in Fig. 10. Closed basin.

7.6. Time scale separations

Let us now consider the typical time scales involved in our experiment. Weak turbulence theory assumes a time scale separation $\tau_l(f) \ll \tau_{nl}(f) \ll \tau_d(f)$, between the linear propagation time, τ_l , the nonlinear interaction time, τ_{nl} , and the dissipation time, τ_d . To our knowledge, such a time scale separation has not been tested experimentally for gravity wave turbulence. The linear propagation time is $\tau_l = 1/f$, whereas $\tau_d(f)$ and $\tau_{nl}(f)$ are inferred from freely decaying experiments using the results of Sect. 7.5. These time scales are displayed in Fig. 14. The dissipative (viscous) linear time scale $\tau_d(f)$ is found to be of the order of 100 s and varies smoothly by a factor 3 within the gravity and capillary frequency ranges. For comparison, a theoretical viscous decay time assuming a dissipation due to a viscous surface boundary layer with an inextensible film (Lamb 1932; van Dorn 1966; Miles 1967; Deike *et al.* 2012) reads

$$\tau_d^{theo} = \frac{2\sqrt{2}}{k(\omega)\sqrt{\omega\nu}}, \quad (7.6)$$

with ν the kinematic viscosity of water, and $k(\omega)$ given by the gravity-capillary dispersion relation. This dissipation comes from the presence of surfactants/contaminants at the interface that leads to an inextensible surface where fluid tangential velocity should be cancelled at the interface. This type of dissipation is known to strongly affect the stability of large scale gravity waves in ocean (Henderson & Segur 2013). For all frequencies, τ_d is found to be much larger than τ_d^{theo} except at the forcing frequencies ~ 1 Hz where both curves intercept. This observation, and the fact that $\tau_d(f)$ varies smoothly compared to $\tau_d^{theo}(f)$, mean that the decay of a largest scale mode (near the forcing scale) transfers energy continuously in time towards small scales. Thus, the decay of all Fourier modes is driven by the viscous decay of a large scale mode as it was observed in small container experiments (Deike *et al.* 2012). Consequently, the estimated nonlinear decay time scales

$\tau_{nl}^g(f)$ and $\tau_{nl}^c(f)$ include a contribution due to the cumulative energy transfer from this large scale mode, in addition to the one by nonlinear wave interactions. Indeed, $\tau_{nl}^g(f)$ is found to roughly decrease as $f^{-3/2}$ in the gravity inertial range, whereas the 4-wave nonlinear interaction time scale reads dimensionally $\tau_{4w}^g \equiv c\epsilon^{-2/3}g^2f^{-3}$ (Connaughton *et al.* 2003; Newell & Rumpf 2011) with ϵ the mean energy flux as estimated in §7.7, and c a non dimensional constant. c is then adjusted to have $\tau_{4w}^g = \tau_{nl}^g \simeq 40$ s at the forcing frequency $f = 1$ Hz. This leads to $\tau_{nl}^g(f) \gg \tau_{4w}^g(f)$ for $f > 1$ Hz, as displayed in figure 14. More interesting, we observe that the scale separation $\tau_l(f) \ll \tau_{4w}^g(f) \ll \tau_d(f)$ is satisfied but in a quite narrow frequency band ($1 < f < 6$ Hz) despite the use of a large basin. Note that a similar analysis can be performed for the capillary regime.

Thus, non-stationary experiments make it possible to estimate for the first time the dissipative and nonlinear time scales in gravity wave turbulence at all scales of the cascade by extrapolating their values from the forcing scale one. We show that an important part of this nonlinear time comes from the cumulative energy transfer from a large scale mode, and thus appears as an upper limit of the 4-wave nonlinear interaction time scale of weak turbulence. This large scale mode thus plays a crucial role in gravity wave turbulence in large basins.

7.7. Estimations of the mean energy flux and Kolmogorov constant

The mean energy flux cascading from large scales to small scales is a key quantity in hydrodynamics turbulence (Pope 2006). In wave turbulence, a way to estimate the mean energy flux ϵ consists of measuring the wave energy decay rate after switching off the wave maker (Denissenko *et al.* 2007; Nazarenko *et al.* 2010). This method gives a good estimate of the mean energy flux provided large scale dissipation is negligible (otherwise the large scale waves loose most of their energy through large scale dissipation and not by transferring energy to smaller scales). Here, the estimation of ϵ is obtained just at the beginning of the energy decay avoiding thus this bias. Assuming no forcing and dissipation, the power budget then reads $dE(t)/dt = -\epsilon$ where $E(t)$ is the wave energy per unit surface and fluid density at time t , and ϵ the mean energy flux per unit surface and density. The energy of linear gravity waves (neglecting capillary ones) averaged over a small time lag reads $E(t) = g\sigma_\eta^2(t)$ with g the acceleration of gravity. Combining both expressions then lead to an estimation of the mean energy flux in the stationary regime ($t \leq 0$)

$$\epsilon = -g \left. \frac{d\sigma_\eta^2(t)}{dt} \right|_{t=0}. \quad (7.7)$$

Figure 15 shows the temporal evolution of $E(t)$ after switching off the wave maker at $t = 0$. The tangent to the curve at $t = 0$ then gives $\epsilon = 100$ (cm/s)³. Note that this value is much smaller than the critical flux $(\gamma g/\rho)^{3/4} \approx 2200$ (cm/s)³ corresponding to the breakdown of weak turbulence at the transition between gravity and capillary regimes (Newell & Zakharov 1992). Estimated values of ϵ in our experiments are such that $\epsilon < (\gamma g/\rho)^{3/4}$. Our estimation of ϵ from the decay of the wave energy is found to increase as expected when the initial wave amplitude increase.

It is now possible, knowing the value of ϵ , to evaluate experimentally the Kolmogorov constant C of Eq. (1.1) from the gravity wave spectrum obtained in the stationary regime at high enough forcing. The inset of figure 15 shows such a spectrum displaying a good agreement with the ω^{-4} power-law scaling expected in the gravity wave turbulence regime and the $\omega^{-17/6}$ one expected in the capillary regime. Using the ω^{-4} fit parameter, the value of ϵ obtained above, and the expression of the non dimensional

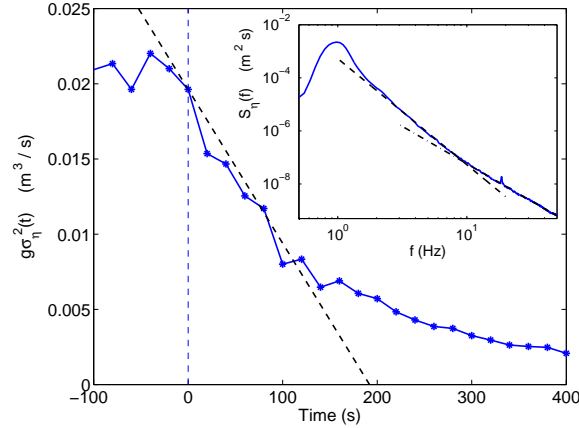


Figure 15: Temporal evolution of the gravity wave energy per unit surface and density. Wave maker is stopped at $t = 0$. Dashed line: tangent at $t = 0$ of slope $\epsilon = 1 \times 10^{-4} \text{ (m/s)}^3$ - see Eq. (7.7). Each value of σ_η is averaged over 20 s. Same initial forcing conditions as in Fig. 10. Closed basin. Inset: Wave power spectrum in the stationary regime for the same forcing conditions. Dashed line: Theoretical weak turbulence spectrum $C\epsilon^{1/3}g\omega^{-4}$ for gravity waves with $C = 1.7$ and $\epsilon = 1 \times 10^{-4} \text{ (m/s)}^3$. Dot-dashed line: $f^{-17/6}$ power-law fit. Closed basin.

Kolmogorov-Zakharov constant (Zakharov & Filonenko 1967a)

$$C = \frac{S_\eta(\omega)\omega^4}{\epsilon^{1/3}g}, \quad (7.8)$$

[$S_\eta(\omega)$ has dimension L^2T and ϵ has dimension L^3/T^3], one finds a value of the constant $C = 1.7$ of same order of magnitude than a theoretical value of 2.75 estimated by Zakharov (2010). Note that Badulin *et al.* (2005) found a numerical constant value of 0.5. Our study then reports the first experimental estimation of the Kolmogorov-Zakharov constant for gravity wave turbulence, the latter being compatible with a recent theoretical value.

8. Conclusion

We have reported results of experiments on gravity wave turbulence in a large basin. The role of the basin boundary conditions have been tested. To this end, an absorbing sloping beach opposite to the wavemaker can be replaced by a reflecting wall. We observe that the wave field properties depend strongly on these boundary conditions. Quasi-one dimensional field of nonlinear waves propagate before to be damped by the beach whereas a more multidirectional wave field is observed with the wall. In both cases, the wave spectrum shows power-law scalings on two decades in frequency (one decade in the gravity range and one in the capillary range). The frequency-power law exponent of the gravity spectrum is found to depend on the nonlinearity level (i.e. forcing strength) with a similar trend in both cases, and up to a value close to -4 at high enough nonlinearity. The physical mechanisms leading to this spectrum at high nonlinearity are likely different: mainly due to propagation of coherent structures in the presence of a beach and to interactions between nonlinear waves in the presence of a wall. The observed steepening of the spectrum at low nonlinearity, in both cases, could be explained by the dissipation

occurring at all scales of the turbulent cascade (see below), a situation not taken into account so far by weak turbulence theory. Small scale intermittency properties of gravity wave turbulence have then been quantified. We found roughly the same value of the intermittency coefficient in presence of a beach or a wall, suggesting the importance of coherent structures in both cases.

We have also studied the non-stationary regime of gravity wave turbulence during its free decay. No self-similar decay is observed in the gravity regime (the frequency power-law exponent of the instantaneous spectrum being dependent on time). We also show that the spectrum Fourier mode amplitudes decay first as a time power law due to nonlinear mechanisms, and then exponentially due to linear viscous damping. A new estimation of the mean energy flux is obtained from the initial decay of wave energy. The Kolmogorov-Zakharov constant is then evaluated for the first time at high nonlinearity, and found to be compatible with a theoretical value estimated by Zakharov (2010). We have also inferred the linear, nonlinear and dissipative time scales at all scales of the cascade. The time scale separation highlights the important role of a large scale Fourier mode (near the forcing scale). Such a large scale mode likely generates non-local interactions that are not also taken into account so far in weak turbulence theory.

Finally, we have found that viscous dissipation occurs at all scales of the cascade, contrary to theoretical hypothesis, and thus induces an ill-defined inertial range between forcing and dissipation. The relative importance of dissipation with respect to nonlinear interactions may explain the observed steepening of the gravity spectrum at low nonlinearity. Indeed, a similar phenomenon of steepening of the spectrum at low nonlinearity has been reported experimentally in wave turbulence on metallic plate (Humbert *et al.* 2013; Miquel *et al.* 2014), and in capillary wave turbulence (Deike *et al.* 2014) when increasing dissipation (e.g. adding dampers on the plate, or working with high enough viscosity fluids), and numerically when reducing the nonlinear interactions (Pan & Yue 2014). Here also, the ratio between dissipation and nonlinearity has to be small enough at all scales to reach a wave turbulence regime. Further theoretical developments introducing realistic empirical dissipating terms in the kinetic equation (as tested numerically by Zakharov *et al.* (2007); WISEGroup (2007) and references therein) would be thus of primary interest for a better understanding of gravity wave turbulence in large basins.

This work was supported by ANR Turbulon 12-BS04-0005. We thank S. Fauve and F. Pétrélis for fruitful discussions. We thank L. Davoust, S. Lambert, C. Laroche and J. Servais for their technical help. We also thank S. Nazarenko and S. Lukaschuk for sending us their data (Nazarenko *et al.* 2010, figure 6 left).

REFERENCES

- BADULIN, S. I., PUSHKAREV, A. N., RESIO, D. & ZAKHAROV, V. E. 2005 Self-similarity of wind-driven seas. *Nonlinear Processes in Geophysics* **12**, 891.
- BANNER, M. L. 1990 Equilibrium spectra of wind waves. *J. Phys. Oceanogr.* **20**, 966.
- BEDARD, R., LUKASCHUK, S. & NAZARENKO, S. 2013a Gravity wave turbulence in a large flume. In *Advances in wave turbulence* (ed. V. Shrira & S. Nazarenko). Singapore : World Scientific.
- BEDARD, R., NAZARENKO, S. & LUKASCHUK, S. 2013b Non-stationary regimes of surface gravity wave turbulence. *Jetp Letters* **87**, 529.
- BERHANU, M. & FALCON, E. 2013 Space-time resolved capillary wave turbulence. *Phys. Rev. E* **89**, 033003.
- BONNEFOY, F. 2005 Modélisation expérimentale et numérique des états de mer complexes. PhD thesis, Université de Nantes et Ecole Centrale de Nantes.

- COBELLI, P., PRZADKA, A., PETITJEANS, P., LAGUBEAU, G., PAGNEUX, V. & MAUREL, A. 2011 Different regimes for water wave turbulence. *Phys. Rev. Lett.* **107**, 214503.
- CONNAUGHTON, C., NAZARENKO, S. & NEWELL, A. C. 2003 Dimensional analysis and weak turbulence. *Physica D* **184**, 86.
- DEIKE, L., BACRI, J. C. & FALCON, E. 2013 Nonlinear waves on the surface of a fluid covered by an elastic sheet. *J. Fluid Mech.* **733**, 394.
- DEIKE, L., BERHANU, M. & FALCON, E. 2012 Decay of capillary wave turbulence. *Phys. Rev. E* **85**, 066311.
- DEIKE, L., BERHANU, M. & FALCON, E. 2014 Energy flux measurement from the dissipated energy in capillary wave turbulence. *Phys. Rev. E* **89**, 023003.
- DENISSENKO, P., LUKASCHUK, S. & NAZARENKO, S. 2007 Gravity wave turbulence in a laboratory flume. *Phys. Rev. Lett.* **99**, 014501.
- DONELAN, M. A., HAMILTON, J. & HUI, W. H. 1985 Directional spectra of wind-generated waves. *Philos. Trans. R. Soc. London A* **315**, 509.
- VAN DORN, W.G. 1966 Boundary dissipation of oscillatory waves. *J. Fluids Mech.* **24**, 769.
- DYACHENKO, A. I., KOROTKEVICH, A. O. & ZAKHAROV, V. E. 2004 Weak turbulent kolmogorov spectrum for surface gravity waves. *Phys. Rev. Lett.* **92**, 134501.
- FALCON, E., FAUVE, S. & LAROCHE, S. 2007a Observation of intermittency in wave turbulence. *PRL* **98**, 154501.
- FALCON, E. & LAROCHE, C. 2011 observation of depth-induced properties in wave turbulence on the surface of a fluid. *EPL* **95**, 34003.
- FALCON, E., LAROCHE, C. & FAUVE, S. 2007b Observation of gravity-capillary wave turbulence. *Phys. Rev. Lett.* **98**, 094503.
- FALCON, E., ROUX, S. G. & AUDIT, B. 2010a Revealing intermittency in experimental data with steep power spectra. *EPL* **90**, 5007.
- FALCON, E., ROUX, S. G. & LAROCHE, S. 2010b On the origin of intermittency in wave turbulence. *EPL* **90**, 34005.
- FALKOVICH, G. E., SHAPIRO, I. Y. & SHTILMAN, L. 1995 Decay turbulence of capillary waves. *EPL* **29**, 1.
- FORRISTALL, G. Z. 1981 Measurements of a saturated range in ocean wave spectra. *J. Geophys. Res.* **86**, 8075.
- FORRISTALL, G. Z. J. 2000 Wave crest distributions: Observations and second-order theory. *Phys. Oceanogr.* **30**, 1931.
- HENDERSON, D. M. & SEGUR, H. 2013 The role of dissipation in the evolution of ocean swell. *J. Geophys. Res.* **118**, 5074.
- HERBERT, E., MORDANT, N. & FALCON, E. 2010 Observation of the nonlinear dispersion relation and spatial statistics of wave turbulence on the surface of a fluid. *Phys. Rev. Lett.* **105**, 144502.
- HUANG, N. E., LONG, S. R., TUNG, C.-C., YUEN, Y. & BLIVEN, L. 1981 A unified two-parameter wave spectral model for a general sea state. *J. Fluid Mech.* **112**, 203.
- HUMBERT, T., CADOT, O., DÜRING, G., JOSSERAND, C., RICA, S. & TOUZÉ, C. 2013 Wave turbulence in vibrating plates: The effect of damping. *EPL* **102**, 30002.
- HWANG, P. A., WANG, D. W., WALSH, E. J., KRABILL, W. B. & SWIFT, R. N. 2000 Airborne measurements of the wavenumber spectra of ocean surface waves. part i: Spectral slope and dimensionless spectral coefficient. *J. Phys. Oceanogr.* **30**, 2753.
- ISSENMANN, B. & FALCON, E. 2013 Gravity wave turbulence revealed by horizontal vibrations of the container. *Phys. Rev. E* **87**, 011001(R).
- JANSSEN, PETER 2004 *The interaction of ocean waves and wind*. Cambridge University Press, New York.
- KAHMA, K. K. 1981 A study of the growth of the wave spectrum with fetch. *J. Phys. Oceanogr.* **116**, 1503.
- KARTASHOVA, E. 1998 Wave resonances in systems with discrete spectra. In *Nonlinear Waves and Weak Turbulence* (ed. V. E. Zakharov), *Amer. Math. Soc. Transl. Ser. 2*, vol. 182, pp. 95–129. Amer. Math. Soc., Providence, RI.
- KITAIGORODSKII, S. A. 1983 On the theory of the equilibrium range in the spectrum of wind-generated gravity waves. *J. Phys. Oceanogr.* **13**, 816.
- KOLMAKOV, G. V., LEVCHENKO, A. A., BRAZHNIKOV, M. YU., MEZHOV-DEGLIN, L. P.,

- SILCHENKO, A. N. & MCCLINTOCK, P. V. E. 2004 Quasiadiabatic decay of capillary turbulence on the charged surface of liquid hydrogen. *Phys. Rev. Lett.* **93**, 074501.
- KOMEN, G. J., CAVALERI, L., DONELAN, M., HASSELMANN, K., HASSELMANN, H., & JANSSEN, P. A. E. M. 1994 *Dynamics and Modeling of Ocean Waves*. Cambridge University Press.
- KOROTKEVITCH, A. O. 2008 Simultaneous numerical simulation of direct inverse cascades in wave turbulence. *Phys. Rev. Lett.* **101**, 074504.
- KUZNETSOV, E.A. 2004 Turbulence spectra generated by singularities. *JETP Lett.* **80**, 83.
- LAMB, H. 1932 *Hydrodynamics*. Springer-Verlag, Berlin.
- LIU, P. C. 1989 On the slope of the equilibrium range in the frequency spectrum of wind waves. *J. Geophys. Res.* **94**, 5017.
- LONG, C. E. & RESIO, D. T. 2007 Wind wave spectral observations in currituck sound, north carolina. *J. Geophys. Res.* **112**, C05001.
- LVOV, Y., NAZARENKO, S. & POKORNI 2006 Discreteness and its effect on water-wave turbulence. *Physica D* **218**, 24.
- MELVILLE, W. K., VERON, F. & WHITE, C. J. 2002 The velocity field under breaking waves: coherent structures and turbulence. *J. Fluid Mech.* **454**, 203.
- MILES, J. W. 1967 Surface-wave damping in closed basins. *Proc. R. Soc. London A* **297**, 459.
- MIQUEL, B., ALEXAKIS, A. & MORDANT, N. 2014 Role of dissipation in flexural wave turbulence: From experimental spectrum to kolmogorov-zakharov spectrum. *Phys. Rev. E* **89**, 062925.
- MIQUEL, B. & MORDANT, N. 2011 Nonstationary wave turbulence in an elastic plate. *Phys. Rev. Lett.* **107**, 034501.
- MOISY, F., RABAUD, M. & SALSAC, K. 2009 A synthetic schlieren method for the measurement of the topography of a liquid interface. *Exp. Fluids.* **46**, 1021.
- NAZARENKO, S. 2006 Sandpile behaviour in discrete water-wave turbulence. *J. Stat. Mech.*, **2**, 1118, L02002.
- NAZARENKO, S. 2011 *Wave Turbulence*. Springer-Verlag, Berlin.
- NAZARENKO, S., LUKASCHUK, S., MCLELLAND, S. & DENISSENKO, P. 2010 Statistics of surface gravity wave turbulence in the space and time domains. *J. Fluids Mech.* **642**, 395.
- NEWELL, A.C. & RUMPF, B. 2011 Wave turbulence. *Annu. Rev. Fluid Mech.* **43**, 59.
- NEWELL, A. C. & ZAKHAROV, V. E. 1992 Rough sea foam. *Phys. Rev. Lett.* **69**, 1149.
- OCHI, M. K. 1998 *Ocean Waves*. Cambridge University Press, Cambridge.
- ONORATO, M., CAVALERI, L., FOUQUES, S., GRAMSTAD, O., JANSSEN, P. A. E. M., MONBALIU, J., OSBORNE, A. R., PAKOZDI, C., SERIO, M., STANSBERG, C. T., TOFFOLI, A. & TRULSEN, K. 2009 Statistical properties of mechanically generated surface gravity waves: a laboratory experiment in a three-dimensional wave basin. *J. Fluid Mech.* **627**, 235.
- ONORATO, M., OSBORNE, A. R., SERIO, M., CAVALERI, L., BRANDINI, C. & STANSBERG, C. T. 2004 Observation of strongly non-gaussian statistics for random sea surface gravity waves in wave flume experiments. *Phys. Rev. E* **70**, 067302.
- ONORATO, M., OSBORNE, A. R., SERIO, M., RESIO, D., PUSHKAREV, A., ZAKHAROV, V. E. & BRANDINI, C. 2002 Freely decaying weak turbulence for sea surface gravity waves. *Phys. Rev. Lett.* **89**, 144501.
- PAN, Y. & YUE, D. K. P. 2014 Direct numerical investigation of turbulence of capillary waves. *Phys. Rev. Lett.* **113**, 094501.
- PERLIN, M., CHOI, W. & TIAN, Z. 2013 Breaking waves in deep and intermediate waters. *Annu. Rev. Fluid Mech.* **45**, 115.
- PHILLIPS, O. M. 1958 The equilibrium range in the spectrum of wind-generated waves. *J. Fluid Mech.* **4**, 426.
- POPE, S. B. 2006 *Turbulent flows*. Cambridge University, Cambridge.
- PUSHKAREV, A., RESIO, D. & ZAKHAROV, V. 2003 Weak turbulent approach to the wind-generated gravity sea waves. *Physica D* **184**, 29.
- ROMERO, L. & MELVILLE, W. K. 2010 Airborne Observations of Fetch-Limited Waves in the Gulf of Tehuantepec. *J. Phys. Oceanogr.* **40**, 441.
- SOCQUET-JUGLARD, H., DYSTHE, K., TRULSEN, K., KROGSTAD, H. E. & LIU, J. 2005 Probability distributions of surface gravity waves during spectral changes. *J. Fluid. Mech.* **542**, 195.

- TAYFUN, M. A. 1980 Narrow-band nonlinear sea waves. *J. Geophys. Res.* **85**, 1548.
- TOBA, Y. 1973 Local balance in the air-sea boundary processes. iii. on the spectrum of wind waves. *J. Ocean Soc. Jpn.* **29**, 209.
- WISEGROUP 2007 Wave modelling the state of the art. *Prog. Ocean.* **75**, 603.
- WRIGHT, W. B., BUDAKIAN, R. & PUTTERMAN, S. J. 1996 Diffusing light photography of fully developed isotropic ripple turbulence. *Phys. Rev. Lett.* **76**, 4528.
- YOKOYAMA, N. 2004 Statistics of gravity waves obtained by direct numerical simulation. *J. Fluid Mech.* **501**, 169.
- ZAKHAROV, V. E. 2010 Energy balance in a wind-driven sea. *Physica Scripta* **T142**, 014052.
- ZAKHAROV, V. E. & FILONENKO, N.N. 1967*a* Energy spectrum for stochastic oscillations of the surface of a liquid. *Sov. Phys. Dokl.* **11**, 881.
- ZAKHAROV, V. E. & FILONENKO, N.N. 1967*b* Weak turbulence of capillary waves. *Journal of applied mechanics and technical physics* **8**, 37.
- ZAKHAROV, V. E., KOROTKEVICH, A. O., PUSHKAREV, A. & RESIO, D. 2007 Coexistence of weak and strong wave turbulence in a swell propagation. *Phys. Rev. Lett.* **99**, 164501.
- ZAKHAROV, V. E., KOROTKEVICH, A. O., PUSHKAREV, A. N. & DYACHENKO, A. I. 2005 Mesoscopic wave turbulence. *JETP Letters* **82**, 487.
- ZAKHAROV, V. E., L'VOV, V. & FALKOVICH, G. 1992 *Kolmogorov spectra of turbulence*. Springer-Verlag, Berlin.
- ZAKHAROV, V. E. & ZASLAVSKY, M. M. 1982 The kinetic equation and kolmogorov spectra in the weak turbulence theory of wind waves. *Izv. Atm. Ocean. Phys.* **18**, 747.